Article | Received 15 June 2026; Revised 18 June 2026; Accepted 18 June 2026; Published 30 June 2026
https://doi.org/10.55092/opr20260004

Supplementary data

Arbitrary eigenmode reshaping induced by distributed non-reciprocity in non-Hermitian systems

Zhaomin Rong[1,†], Yu Chen[2,†], Yanan Bai[1], Tiejun Cui[2,*], Lei Zhou[3,4,5,*], Shuo Liu[2,*] and Shaojie Ma[1,3,5,*]

[1] College of Future Information Technology, Fudan University, Shanghai 200433, China
[2] State Key Laboratory of Millimeter Waves, Southeast University, Nanjing 210096, China
[3] Shanghai Key Laboratory of Metasurfaces for Light Manipulation, Shanghai 200433, China
[4] State Key Laboratory of Surface Physics and Department of Physics, Fudan University, Shanghai 200433, China
[5] Key Laboratory of Micro and Nano Photonic Structures (MOE), Fudan University, Shanghai 200433, China

† These authors contributed equally to this work.

* Correspondence authors; E-mails: tjcui@seu.edu.cn (T.C.); phzhou@fudan.edu.cn (L.Z.); liushuo.china@seu.edu.cn (S.L.); shaojiema@fudan.edu.cn (S.M.).

1. Theoretical analysis

1.1. 1D nearest-neighbor TBM model

To demonstrate the ubiquity of the non-Hermitian reshaping engineering, we investigate a 1D non-reciprocal nearest-neighbor Tight-Binding Model (TBM) under open boundary conditions (OBCs). This model elucidates the transition behavior of particles within a 1D non-reciprocal atomic chain. By considering only nearest-neighbor interactions and neglecting beyond-nearest-neighbor couplings, the dynamics can be described using a single-particle Hamiltonian.

$$\hat{H} = \sum_{n=1}^{N} w_n^{(1)} |n+1\rangle\langle n| + w_n^{(2)} |n\rangle\langle n+1| + l_n |n\rangle\langle n| \tag{S1}$$

Here, $|n\rangle$ represents the quantum states where a particle is located on the n-th unit cell. Such an atomic chain comprises N unit cells, and the flexibility of this model manifests in the parameter $w_n^{(1)}$ and $w_n^{(2)}$, where the non-reciprocal transition coefficients between adjacent sites can be entirely inhomogeneous and arbitrary.

By introducing non-reciprocity into the hopping coefficients through $w_n^{(1)} \neq \mathrm{conj}(w_n^{(2)})$, a non-Hermitian TBM model can be constructed. A common definition sets the hopping coefficient $w_n^{(1)} = w_n + \delta$ in one direction while setting the other $w_n^{(2)} = w_n$. In this article, we modify the hopping coefficient to the right as $w_n^{(1)} = w_n \cdot e^{\kappa_n}$ and to the left as $w_n^{(2)} = w_n \cdot e^{-\kappa_n}$. These two formulations are mathematically equivalent when $w_n^{(2)} = w_n \cdot e^{-\kappa_n}$. The item κ_n is used to characterize the distribution of arbitrary non-reciprocity in the system.

$$\mathbf{H} = \sum_{m,n} H_{NR,mn} \cdot |m\rangle\langle n| = \sum_n w_n (e^{-\kappa_n - i\phi_n}|n\rangle\langle n+1| + e^{\kappa_n + i\phi_n}|n+1\rangle\langle n|) + l_n|n\rangle\langle n| \tag{S2}$$

For the special case of $N = 4$, the Hamiltonian of such a non-Hermitian model can be expressed as:

$$H_{NR} = \begin{pmatrix} l_1 & w_1 e^{-\kappa_1 - i\phi_1} & 0 & 0 \\ w_1 e^{-\kappa_1 + i\phi_1} & l_2 & w_2 e^{-\kappa_2 - i\phi_2} & 0 \\ 0 & w_2 e^{-\kappa_2 + i\phi_2} & l_3 & w_3 e^{-\kappa_3 - i\phi_1} \\ 0 & 0 & w_3 e^{-\kappa_3 + i\phi_3} & l_4 \end{pmatrix} \tag{S3}$$

The eigenvalues of the Hamiltonian can be obtained by solving the characteristic equation $|H - E \cdot I| = 0$, where I is the identity matrix. The matrix associated with this determinant is known as a nth-order *tridiagonal matrix* in mathematics:

$$f_n = \begin{vmatrix} a_1 & b_1 & & & \\ c_1 & a_2 & \ddots & & \\ & \ddots & \ddots & \ddots & \\ & & \ddots & a_{n-1} & b_{n-1} \\ & & & c_{n-1} & a_n \end{vmatrix} \tag{S4}$$

which possesses several interesting properties that can simplify the calculation of eigenvalues. It is revealed that b_n and c_n never appear separately in this determinant and they always emerge in pairs as products.

Proof

Assuming that neither $|H_{n-1} - EI_{n-1}|$ nor $|H_{n-2} - EI_{n-2}|$ contains terms involving κ. From Equation S5, it follows that:

$$|H_n - EI_n| = (a_{n-1} - E) \cdot |H_{n-1} - EI_{n-1}| - b_{n-1}c_{n-1} \cdot |H_{n-2} - EI_{n-2}|,$$

where $b_{n-1} = w_{n-1}e^{\kappa_{n-1}}$, $c_{n-1} = w_{n-1}e^{-\kappa_{n-1}}$, giving $b_{n-1} \cdot c_{n-1} = w_{n-1}^2$. Since b_{n-1} and c_{n-1} always appear as a product, the dependence on κ_n is exactly eliminated.

As the induction bases, we note that

$$|H_2 - EI_2| = E^2 - w_1^2$$

$$|H_3 - EI_3| = -E^3 + Ew_1^2 + Ew_2^2$$

neither of which contains terms associated with κ_n. Consequently, by induction, $|H_n - EI_n|$ is independent of κ for any tridiagonal matrix H_n.

The sequence f_n satisfies the recurrence relation:

$$f_n = a_n \cdot f_{n-1} - c_{n-1}b_{n-1} \cdot f_{n-2} \tag{S5}$$

The subscript indicates the order of the tridiagonal matrix. It can be mathematically proved that

$|H - E \cdot I|$ does not contain any terms related to κ.

Having established that the eigenvalue spectrum of the non-Hermitian Hamiltonian under OBCs is rigorously independent of the imaginary gauge potential κ, this spectral invariance can be made explicit through a diagonal similarity transformation that maps the non-Hermitian Hamiltonian to a Hermitian counterpart. This transformation serves as the *explicit realization* of the spectral invariance proved above, rather than its premise: the existence of a unique diagonal metric is a consequence of the tridiagonal structure of the 1D nearest-neighbor Hamiltonian under OBCs. The relation can be expressed as:

$$H_{NR} = T H_R T^{-1} \tag{S6}$$

where T represents the similarity transformation matrix. In the nearest-neighbor TBM model discussed earlier, T can be a diagonal matrix $\hat{T} = \mathrm{diag}(t_1, t_2, \cdots)$ and $H_{NR,mn} = {t_m}^{-1} t_n H_{R,mn}$, where $H_{NR,mn}$ is nonzero only when $m = n \pm 1$. The spatially distributed non-reciprocity κ_n is directly related to the recursive relation for t_n:

$$t_{n+1} = e^{\kappa_n} \cdot t_n \tag{S7}$$

This recursive relation completely determines the expression of the diagonal similarity matrix T. Such a similarity transformation can be used to modify the eigenfunctions. As a result, regardless of the choice of spatial function of the non-Hermitian coefficients κ_n, we can achieve precise theoretical predictions of the modified eigenfunctions. This undoubtedly paves the way for new possibilities in non-Hermitian modulation.

This similarity transformation admits a natural geometric interpretation: the diagonal matrix T encodes a nontrivial metric on the Hilbert space, with t_n determined by the distribution of non-reciprocity $\kappa(n)$ (also interpreted as the imaginary gauge potential). From this perspective, NHRE physically corresponds to engineering the Hilbert-space metric while preserving the spectrum.

Crucially, this metric engineering via off-diagonal non-reciprocity is conceptually independent of other forms of non-Hermiticity, such as on-site gain and loss. Under OBCs, the similarity transformation completely absorbs all non-reciprocity into the metric T, reducing H_{NR} to an equivalent reciprocal Hamiltonian H_R that may still contain diagonal gain/loss terms. Thus, non-reciprocity shapes the eigenmode profiles without affecting the eigenvalues, while gain and loss primarily influence the spectral properties.

Regarding topology, although eigenstate-based topological invariants may change due to the non-unitary nature of T, the spectral fingerprints of topology, such as the robust existence and energy position of in-gap boundary states, are preserved under the similarity transformation. These spectrally determined topological features can therefore be fully analyzed through the equivalent reciprocal Hamiltonian H_R.

1.2. General TBM models

In the above derivation, we have relied on the mathematical properties of tridiagonal matrices. However, the Hamiltonian matrix is generally not tridiagonal. This implies that our derivation cannot be directly extended to cases involving next-nearest-neighbor interactions or higher dimensions.

It is important to clarify the scope of this restriction. The above limitation applies only to the *inverse problem*, in which one attempts to extract a Hermitian parent Hamiltonian and a well-defined metric from an arbitrarily prescribed non-reciprocal Hamiltonian. This inverse problem indeed becomes over-constrained once next-nearest-neighbor or longer-range couplings are present, because the metric extracted from one set of off-diagonal elements would generally fail to be compatible with the others. However, this restriction does *not* apply to the *forward construction* that underlies all of our higher-dimensional and beyond-nearest-neighbor results: starting from a known reference Hamiltonian and a desired envelope function, one applies the diagonal similarity transformation to construct the modulated non-reciprocal Hamiltonian. This forward approach remains fully operational in arbitrary dimensions and beyond nearest-neighbor couplings, as elaborated below.

Nevertheless, some aspects of the above results still hold in more general cases. While we can NOT guarantee that an arbitrary non-Hermitian Hamiltonian can always be transformed into a Hermitian one with well-defined dispersion spectrum and topological property through the similarity transformation (this conclusion is inevitable; otherwise, no new physics would emerge from non-Hermitian systems), it is still possible to apply a diagonal similarity transformation T to a well-defined system H_R. This Hamiltonian H_R is not restricted to a Hermitian one but can be any TBM model with known properties. Consequently, a corresponding non-reciprocal Hamiltonian $H_{NR} = T^{-1} H_R T$ can be constructed, which inherits the dispersion spectrum and the spectral fingerprints of topology (e.g., the presence of in-gap boundary states) of the base Hamiltonian H_R, while offering arbitrarily adjustable mode distribution. Eigenstate-based topological invariants, however, may change due to the non-unitary nature of the transformation. These features can be effectively applied to specific mode control applications, such as the design of laser cavities.

2. Numerical verifications

2.1. 1D NH-SSH model

The theoretical analysis yielded promising results, demonstrating that non-Hermitian manipulations can be applied to arbitrary models while preserving their topological properties. In the following numerical calculations, we will validate these theoretical findings using the non-Hermitian SSH model and explore the intriguing aspects of this manipulation approach.

Here, we consider two typical models. When taking $\kappa = \kappa_0$ and setting alternating hopping amplitudes $w_{2i} = w$ and $w_{2i+1} = v$, this scenario corresponds to the prototypical model of the non-Hermitian skin effect (NHSE) introduced by Yao and Wang in 2018. Within the NHRE framework, this represents the special case of a uniform imaginary gauge potential, where the envelope function T can be solved as $t_n = C \cdot \exp(\kappa_0 n)$, which directly defines an exponential metric that localizes all eigenstates at one boundary, as shown in Figure S1a,b. Furthermore, from the corresponding Hermitian Hamiltonian, it is evident that the topological transition point occurs at $v = w$, consistent with the result obtained from the generalized Brillouin zone theory.

In the second model, we choose $\kappa_n = -\kappa_0 \cdot \Theta(n_0 - n)$ as a step function, with the non-Hermitian modulation applied only to the region where $n \leqslant n_0$. Therefore, T can be expressed as $t_n = \exp[-\kappa_0 (n - n_0)]$ when $n \leqslant n_0$ and $t_n = 1$ when $n > n_0$. Previous article [38] combined two SSH models with different topological characteristics to induce edge states at the domain wall,

where the index n_0 denotes the interface separating the two models. These edge states can be represented by $\psi(n) = C' \exp[\sigma \cdot (n - n_0)]$ when $n \leqslant n_0$, where σ denotes the decay rate of the edge state. When the parameters are appropriately chosen, the envelope function t_n applied to the edge states precisely counteracts the intrinsic decay of the topological edge state, delocalizing it into an extended mode that occupies the entire bulk lattice. This is fully consistent with the conclusions of the previous article on the non-Hermitian morphing effect, as shown in Figure S1c,d.

A slightly more complex scenario than a piecewise κ is when $\kappa(n)$ is linearly distributed, *i.e.* $\kappa_n = -\alpha \cdot (n - r)$, where α and r are modulation parameters. According to Equation S7, we can derive the expression for t_n in this case:

$$t_n = C \exp\left[-\frac{1}{2}\alpha (n - n_c)^2\right] \tag{S8}$$

Here, $n_c = r - 3/2$ represents the central position of the modulated function, and C is a constant generated during the calculation that is not of concern. If α is positive, the envelope function t_n essentially becomes a Gaussian function.

Assuming the expression for the edge state satisfies $\psi(n) = A \exp(-\sigma n)$, where σ represents the decay rate of the edge state. According to Equation S7, multiplying t_n by the edge state wave function yields

$$\psi(n) = C' \exp\left[\kappa_0 \left(n - n_c - \frac{\sigma}{2\kappa_0}\right)^2\right] \tag{S9}$$

This is the analytical expression for the modulated wave function, indicating that the edge state is modulated into a Gaussian function and translated by a certain distance, shifting from the boundary into the bulk, as shown in Figure 1e.

Figure S2 illustrates the manipulation of bulk and edge states, respectively. Both the bulk states in Figure S2a and edge states in Figure S2b are shifted towards the center under the influence of the Gaussian shaped envelope function t_n depicted in Figure S2c. Notably, the positions of the modulated bulk state in Figure S2d are not fully correlated with the edge state in Figure S2e. The bulk states are confined to the center while the edge states can still be shifted to different positions under fine-tuning of the system parameters. This indicates that, although NHRE acts via a global transformation that reshapes all modes simultaneously, different mode classes can exhibit effective mode selectivity due to their distinct pre-existing spatial profiles in the parent Hermitian Hamiltonian. This emergent selectivity further enhances the tunability of NHRE for mode engineering applications.

To further validate the robustness of spectral fingerprints of topological edge states under NHRE, we performed additional numerical simulations incorporating perturbations. Specifically, for the case with $\alpha = 0.04$, we applied 2%, 5%, and 10% normally distributed tolerance to all capacitors in the circuit and performed 100 simulations for each tolerance level. The results, summarized in Figure S3, demonstrate that the eigenfrequencies corresponding to the edge states remain well separated from the bulk states across all disorder realizations, with no instance of merging into the bulk continuum. The spatial profiles of the edge states, while exhibiting minor variations due to disorder, consistently retain their localization characteristic at specific positions.

These findings confirm that the spectral isolation of topological edge states, inherited from the parent Hermitian Hamiltonian via the spectrum-preserving NHRE transformation, renders them robust against a finite level of structural perturbations. The non-reciprocal modulation reshapes their spatial envelopes without compromising their topological robustness.

2.2. 2D NH-BBH model

While our previous calculations validated the framework in 1D, we now apply it to the 2D BBH model to demonstrate its broader applicability to more general systems. The most notable feature of the BBH model is the corner-localized modes that emerge within the bandgap. We define the field distribution of the corner state as $\psi(n)$, and the target wavefunction as $\psi'(n)$. Consequently, the envelope function t_n can be expressed as $t_n = \psi'(n)/\psi(n)$. This similarity transformation introduces a non-Hermitian modulation to all Hamiltonian elements connected to site n. As the modulation simply rescales the original Hermitian couplings, the tight-binding connectivity is preserved while the coupling strengths are modified. In the BBH model, the resulting Hamiltonian thus retains only nearest-neighbor interactions, but with almost all couplings rendered nonreciprocal.

This regulation allows for arbitrary control over a specific state. In the main text, we numerically demonstrated arbitrary manipulation of the field distribution of a corner state, localizing the field at another corner, two corners, the center, or any desired field configuration.

3. Topological circuit verification

3.1. Generation of non-reciprocity in circuit systems

Non-reciprocal coupling in the topological circuit is realized via unidirectional coupling capacitors. As depicted in Figure S4, each coupler comprises a voltage follower in series with one coupling capacitor, placed in parallel with another coupling capacitor. The voltage follower is implemented via an operational amplifier (Op-Amp) configured with negative feedback. Exploiting the virtual short and virtual open circuit conditions at the Op-Amp's input terminals, the left-side current path through the capacitor is blocked, while the right-side path remains conductive, as shown in Figure S4. This asymmetry produces different effective conductance, $J_{ab} = I_1/(V_b - V_a)$ and $J_{ba} = -(I_1 + I_2)/(V_a - V_b)$, between the connected nodes, thereby establishing non-reciprocal behavior.

In our circuit setup, we can reliably produce $\kappa(n)$ values between -4 and 4, corresponding to coupling ratios $\exp(\pm\kappa)$ ranging from approximately 0.018 to 55. This range is fundamentally limited by the achievable minimum and maximum capacitance values in the circuit. In particular, the lower bound of $|\kappa|$ is constrained by the fact that the smallest capacitance cannot be made arbitrarily small, as it would then become comparable to the parasitic capacitance of the circuit, compromising the accuracy and non-reciprocal behavior. Within this range, the deviation from ideal exponential scaling is within experimentally acceptable limits across the frequency range of interest, as evidenced by the excellent agreement between measured and theoretical mode profiles shown in Figure 4. This comfortably accommodates all modulation profiles demonstrated in our work.

3.2. Non-Hermitian model analysis via impedance measurements

For Hermitian topological circuits, the eigenstates can be directly extracted from self-impedance measurements. The circuit Laplacian J is generally expressed as:

$$J(w)=i\omega C\cdot H_R+\left(i\omega C_t+\frac{1}{i\omega L_t}\right)I=i\omega C\cdot[H_R-\lambda(\omega)I] \tag{S10}$$

Here, H_R is the effective Hamiltonian of the implemented Hermitian SSH model circuit. C and C_t are the Laplacians corresponding to the coupling capacitor and the node resonance capacitor, respectively. Given that H_R is Hermitian, it is diagonalizable by a unitary matrix Ψ composed of all its orthonormal eigenstates:

$$J(w)=iwC\cdot[\Psi D\Psi^{\dagger}-\lambda(w)\Psi\Psi^{\dagger}]=iwC\cdot\Psi[D-\lambda(w)]\Psi^{\dagger} \tag{S11}$$

Here, D is a diagonal matrix containing all the eigenvalues of H_R. Consequently, the impedance matrix Z, being the inverse of the admittance, takes the form:

$$Z(w)=[J(\omega)]^{-1}=\frac{1}{iwC}\cdot\Psi[D-\lambda(\omega)I]^{-1}\Psi^{\dagger} \tag{S12}$$

Denoting E_n the n-th eigenstate of Hamiltonian H_R, the self-impedance Z_{aa} at node a is therefore analytically given by:

$$Z_{aa}=[J^{-1}(\omega)]_{aa}=\frac{1}{i\omega C}\cdot\sum_n\frac{|\Psi_{an}|^2}{E_n-\lambda(\omega)} \tag{S13}$$

Analysis of Equation S13 reveals that a resonance peak in Z_{aa} arises when the value $\lambda(w)$ matches a typical eigenvalue E_n of the Hamiltonian H_R, as the denominator approaches zero (remaining finite experimentally due to inherent resistance). This peak signifies the excitation of the n-th mode. By scanning frequency and measuring self-impedance at each circuit node, one directly maps the squared modulus of the eigenstates $|\Psi_{an}|^2$ for each mode n.

Within the non-Hermitian framework considered here, Hermitian and non-Hermitian Hamiltonians are mathematically connected via a similarity transformation, and their modes can be obtained through the transformation:

$$H_{NR}=TH_RT^{-1}=T\Psi\cdot D\cdot\Psi^{\dagger}T^{-1} \tag{S14}$$

Substituting this expression into Equation S11 yields

$$J(\omega)=i\omega C\cdot T\Psi\cdot[D-\lambda(\omega)]\cdot\Psi^{\dagger}T^{-1} \tag{S15}$$

Consequently, the self-impedance Z_{aa} for this non-Hermitian system is obtained as:

$$Z_{aa}=[J^{-1}(\omega)]_{aa}=\frac{1}{i\omega C}\cdot\sum_n\left(\frac{t_a\Psi_{an}\cdot\Psi_{na}^{\dagger}t_a^{-1}}{E_n-\lambda(\omega)}\right)=\frac{1}{i\omega C}\cdot\sum_n\frac{|\Psi_{an}|^2}{E_n-\lambda(\omega)} \tag{S16}$$

Crucially, for non-Hermitian models defined in this manner, self-impedance measurements reproduce the eigenstates of the corresponding Hermitian model, rather than the true eigenmodes of the non-Hermitian system, as shown in Figure S5.

To probe the intrinsic non-Hermitian properties, we employ the mutual impedance Z_{ab}. Similar to Equation S16, Z_{ab} can be analytically expressed as:

$$Z_{ab} = \frac{1}{i\omega C} \cdot \sum_n \frac{t_a \Psi_{an} \cdot \Psi_{bn}^* t_b^{-1}}{E_n - \lambda(\omega)} \tag{S17}$$

Similarly, the denominator $E_n - \lambda(\omega)$ produces a resonance peak when $E_n \approx \lambda(\omega)$. In the ideal model without parasitic resistance, the resonance peaks would diverge. To prevent numerical divergence, we manually introduce an additional imaginary component into $\lambda(\omega)$, *i.e.*, $\tilde{\lambda}(\omega) = \lambda(\omega) - i\eta$, with η a positive infinitesimal. At $E_n = \lambda(\omega_n)$, the summation is dominated by the n-th mode, resulting in:

$$[Z(\omega_n)]_{ab} = \left(- \frac{\Psi_{bn}^* t_b^{-1}}{\eta \omega_n C} \right) \cdot t_a \Psi_{an} \tag{S18}$$

Here, $\Psi_{an}' = t_a \Psi_{an}$ represents exactly the eigenstate of the non-Hermitian Hamiltonian H_{NR}, with a normalization factor depending on the excitation position b. By fixing b (e.g., $b = 1$) and scanning position a, the spatial profile of the eigenstate Ψ_{an}' can be reconstructed.

Importantly, the normalization factor depends on the choice of excitation site b through the eigenstate component Ψ_{bn}^*. Consequently, while the resonant frequency, *i.e.*, E_n, remains unchanged for different choice of b, the relative intensity distribution across different modes varies, as shown in Figure S6. To minimize the dependence of the spectral profile on the specific choice of b, we summed the mutual impedance and defined $\widetilde{Z}_a$ as $\widetilde{Z}_a = \Sigma_b |Z_{ab}|$ over multiple excitation positions b to characterize the circuit's spatial and frequency response. The $\widetilde{Z}_a$ spectrum reveals all mode frequencies and spatial profiles with nearly uniform intensity, as shown in Figure S6d.

3.3. Data processing: impedance correction

To clearly identify the modulation effect in our NHRE experiment, we deliberately selected a large value for α. This results in a large ratio of the coupling capacitance C to the resonance capacitance C_t at each node. Consequently, the resonant frequencies are restricted to a very narrow frequency band. Therefore, the loss-induced broadening of the impedance peaks results in significant spectral overlap among the bulk modes, making them indistinguishable in the measured $\tilde{Z}_a$ spectrum.

Here, we introduce a compensation method to recover the original system information and resolve spectral overlap, even when bulk states merge due to low Q-factors. Although resistances are present in inductors, capacitors, and interconnects, parasitic inductor resistance dominates, as confirmed by individual-component measurements. Our compensation strategy therefore begins by considering a simplified model that accounts for these dominant inductor losses, before generalizing to a fully data-driven calibration that captures all loss sources without assumptions.

The ideal admittance matrix, also known as circuit Laplacian, is defined by Equation S10. The incorporation of resistive effects modifies this expression as follows:

$$J(\omega) = i\omega C \cdot H_{NR} + \left(i\omega C_t + \frac{1}{i\omega L_t + R_t} \right) \cdot I = i\omega C \cdot [H_{NR} - \lambda'(\omega) \cdot I] \tag{S19}$$

where the resonance frequency scale item $\lambda'(w)$ becomes $\lambda'(\omega) = -C_t/C + 1/[(\omega L_t - iR_t)\omega L]$, which is complex due to the parasitic inductor resistance R_t. Therefore, the mutual impedance Z_{ab} can be analytically derived:

$$Z_{ab} = \frac{1}{i\omega C} \cdot \sum_n \left(\frac{\Psi_{nb}^{\dagger} t_b^{-1}}{E_n - \mathrm{Re}[\lambda(\omega)] - i\,\mathrm{Im}[\lambda(\omega)]} \right) \cdot \Psi_{an}' \tag{S20}$$

This parasitic resistance broadens Z_{ab} spectrum into Lorentzian lineshapes. While moderate loss is necessary for practical observation (avoiding delta-function singularities), excessive loss leads to mode overlap, making individual modes indistinguishable in experiments.

Once the specific form of loss contributions in the admittance matrix is identified, they can be computationally removed. This approach is conceptually analogous to the complex frequency excitation used in recent works to compensate for material loss, but is implemented here through a customized procedure.

In our experiment, mutual impedance spectrum was measured via transmission coefficient S_{21} across all nodes using a vector network analyzer (VNA). The corresponding admittance matrix was subsequently derived from the measured S-matrix:

$$J = z_0^{-1} \cdot (I - S) \cdot (I + S)^{-1} \tag{S21}$$

The desired impedance matrix Z is then obtained by inverting the admittance matrix. To account for and remove the influence of inherent losses, we numerically subtracted the loss contribution using the expression:

$$J(w) = z_0^{-1} \cdot [I - S(\omega)] \cdot [I + S(\omega)]^{-1} + \mathrm{diag}[J_C(n,\omega)] \tag{S22}$$

where $J_C(n,w)$ represents the loss compensation matrix, which is applied to account for and subtract experimental losses from the measured data.

In principle, the compensation strategy employs a uniform gain J_C across the entire system, which is theoretically derivable from a fixed resistance parameter:

$$J_C = \left(-\frac{1}{i\omega L_t + R_C} + \frac{1}{i\omega L_t} \right) \cdot I = \frac{R_C}{i\omega L_t (i\omega L_t + R_C)} \cdot I \tag{S23}$$

Here, R_C serves as an approximation to the actual parasitic resistance R_t in the circuit.

However, this approach yields suboptimal performance due to the intrinsic spatial non-uniformity of losses, applying a single compensation value leads inevitably to over-correction at some nodes and under-correction at others. Moreover, R_t itself exhibits strong frequency dependence, varying significantly across both high and low frequencies. Relying on a constant formula of J_C for compensation is therefore fundamentally limited. Furthermore, since J_C is typically chosen arbitrarily, the compensation process introduces a degree of subjectivity, which undermines the reproducibility of the results.

To address these issues, we propose an experimental calibration protocol based on the measured diagonal elements J_{nn} of the impedance matrix, which generalizes to a fully data-driven calibration that captures all loss sources without assumptions. In a lossless circuit, J_{nn} must be purely imaginary, a fundamental result of circuit theory that holds for a passive, lossless network, independent of specific component values or model assumptions. Therefore, we introduce a compensating resistance $J_C(n,\omega)$ to cancel out their measured real parts, retaining only the imaginary components. The value of $J_C(n,\omega)$ is determined directly from experimental data, thereby eliminating any arbitrary choices in the data processing procedure. Moreover, the resistance value autonomously self-adjusts according to both frequency and spatial position, as governed by the intrinsic response of the circuit system. Crucially, it inherently accounts for losses from all possible sources within the entire circuit—rather than being

restricted only to parasitic resistance in inductive components, as is used in simplified models. This adaptive compensation effectively suppresses additional errors that would arise from idealized theoretical models.

A comparison of different processing methods is presented in Figure S7. It can be observed that the calibration scheme based on J_{nn} reproduces the theoretical results with excellent agreement, yielding a clear spectral profile while eliminating any arbitrariness in the numerical processing.

We further verify the robustness and determinism of the compensation method numerically. On the theoretical side, we introduced random losses comparable to the experimental levels into the theoretical model, along with circuit component tolerances and realistic measurement uncertainties. Under these conditions, the algorithm consistently recovers the lossless eigenfrequencies and mode profiles. Multiple independent evaluations of the same circuit state yield compensated $\tilde{Z}_a$ spectra that overlap nearly perfectly (see Figure S8). These results confirm the validity and robustness of the compensation method, demonstrating its capability to faithfully recover the lossless response under realistic experimental conditions.

4. Non-Hermitian modulated CROWs

A single optical ring resonator supports two degenerate whispering-gallery modes at the $n-th$ characteristic frequency ω_n: the clockwise (CW) and counterclockwise (CCW) modes, whose field profiles take the form $E \cdot exp(ik_n\theta)$ and $E \cdot exp(-ik_n\theta)$, respectively. For computational efficiency, we model the structure using a two-dimensional full-wave simulation.

In the Hermitian case, the coupled resonant optical waveguides (CROWs) are formed by linking adjacent ring resonators through a link ring, which couples modes of the same spin (CW or CCW) between neighboring sites. This coupled system still supports two degenerate modes, the CW and CCW modes. To avoid spectral overlap and suppress CW–CCW conversion, the link ring is deliberately designed with a different eigenfrequency. By tuning its radius, the link ring's resonance is shifted outside the operational band, ensuring that its own mode does not interfere with the CROW dynamics.

To introduce non-reciprocity, gain and loss are incorporated into different sections of the link ring, with the upper segment serving as the gain region and the lower segment as the loss region, as shown in Figure S9a. For a CW mode propagating from left to right, the field always passes through the loss section of the link ring, resulting in a reduced coupling strength to the next resonator. Conversely, when propagating from right to left, the field traverses the gain region, leading to an enhanced coupling strength. Consequently, the CW mode inside the site rings experiences direction-dependent coupling strengths, establishing a non-reciprocal interaction. It is worth noting that the CCW mode exhibits the same behavior, but with the roles of gain and loss reversed. For these two modes, the system forms two separate single-chain SSH models with opposite non-reciprocal interactions, as illustrated in Figure S9b. Two degenerate eigenvalues at each frequency correspond to the CW and CCW eigenstates, respectively.

However, the gain and loss in the link ring slightly modify the material impedance, inducing a small amount of reflections from CW to CCW at the interface, thereby generating coupling between the two modes. Under weak non-Hermitian modulation, this coupling is negligible. However, when the gain and loss become sufficiently strong, a small coupling emerges, lifting the degeneracy and modifying the system's eigenstate properties. Consequently, the two modes are mixed in the resulting eigenstates. This interaction can be modelled by a two-chain non-Hermitian SSH model, where each site features an

additional coupling $t_\perp$ between the CW and CCW modes, as illustrated in Figure S9c. Once the weak coupling is introduced, the degeneracy is gradually lifted, altering the characteristics of the modes.

In Figure S9d–f, we show the energy spectra from both full-wave simulations and the uncoupled/coupled two-chain SSH TBMs. The coupled TBMs reproduce the exact level-splitting behavior observed in the simulations, with slight shifts in eigenfrequencies relative to the Hermitian Hamiltonian. These shifts vanish completely when $t_\perp$ is reset to zero, confirming that the source of the discrepancy with NHRE predictions lies in this offset.

Nevertheless, even with such shifts, NHRE remains valid. To illustrate this, we show the mode corresponding to the smallest eigenvalue and project it onto the CW and CCW field profiles, $E \cdot e\exp(\pm ik_n\theta)$, to resolve the spatial distributions of the CW and CCW components separately, as shown in Figure S9g–i. The results demonstrate excellent agreement between simulation and the coupled TBMs. Despite the mode coupling, NHRE still modulates the CW component toward the center while the CCW component accumulates at the boundaries, consistent with the modulation behavior of the TBM without additional coupling. This confirms that NHRE effectively controls mode localization even in the presence of inter-mode coupling.

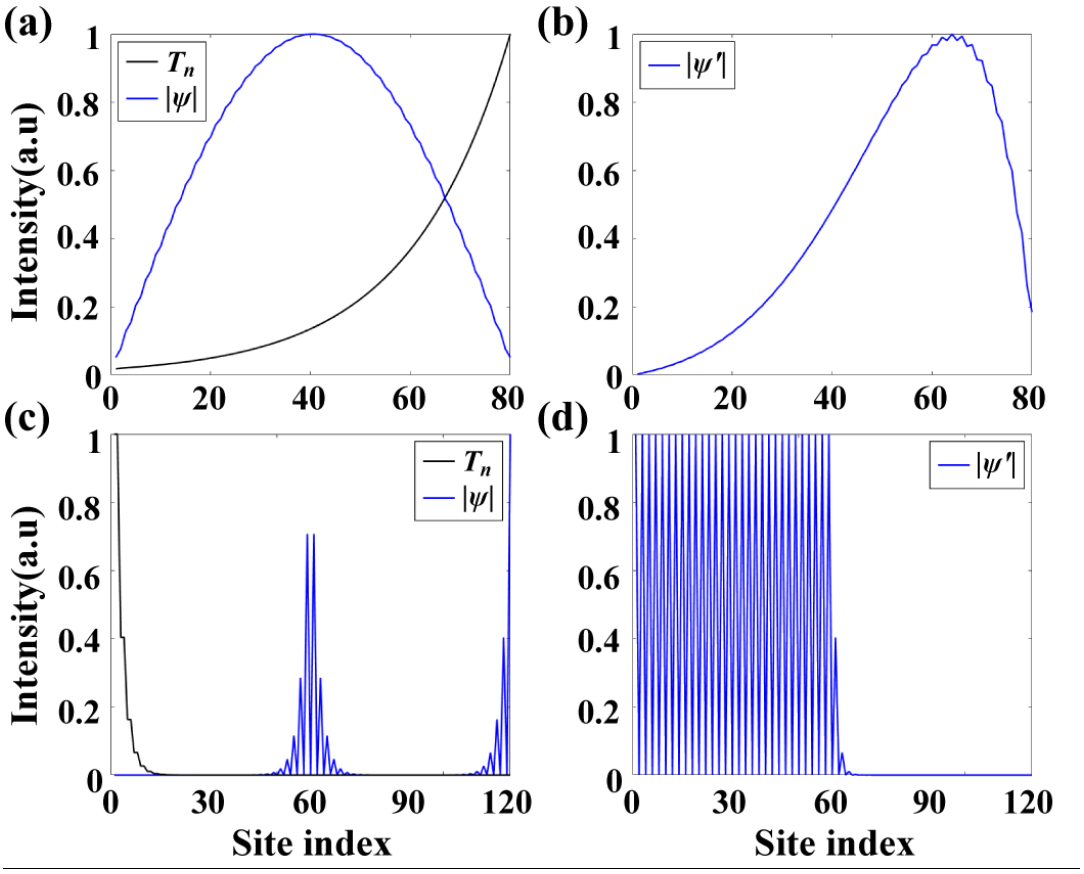

Figure S1. Illustration of two typical models of NHRE: **(a, b)** Schematic diagram of the non-Hermitian skin effect, where the blue solid line in **(a)** represents a representative bulk state of the corresponding Hermitian SSH model, and the black solid line denotes the envelope function t_n. The product of these two functions results in the solid line in **(b)**, which signifies the bulk states of the non-Hermitian SSH model, exhibiting the characteristic exponential localization at the boundary—a hallmark of NHSE arising from a constant non-reciprocity that defines an exponential metric; **(c, d)** Schematic

diagram of the non-Hermitian morphing effect, where the blue solid line in **(c)** depicts the edge states at the domain wall, and the black solid line again represents the envelope function t_n. Their product yields the blue solid line in **(d)**, corresponding to the delocalized topological zero mode that occupies the entire bulk lattice.

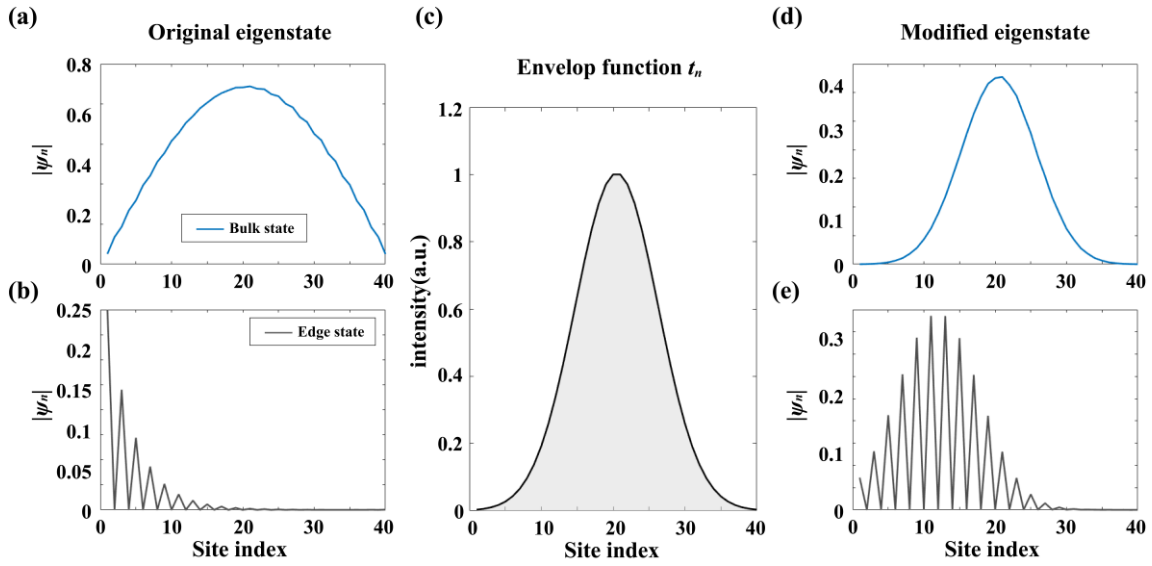

Figure S2. Manipulation of bulk and edge states via NHRE: **(a, b)** Spatial distribution of the **(a)** bulk state and **(b)** edge state in the original Hermitian Hamiltonian; **(c)** Envelope function t_n; **(d, e)** Spatial distribution of the modified **(d)** bulk state and **(e)** edge state after the NHRE transformation in the non-Hermitian Hamiltonian.

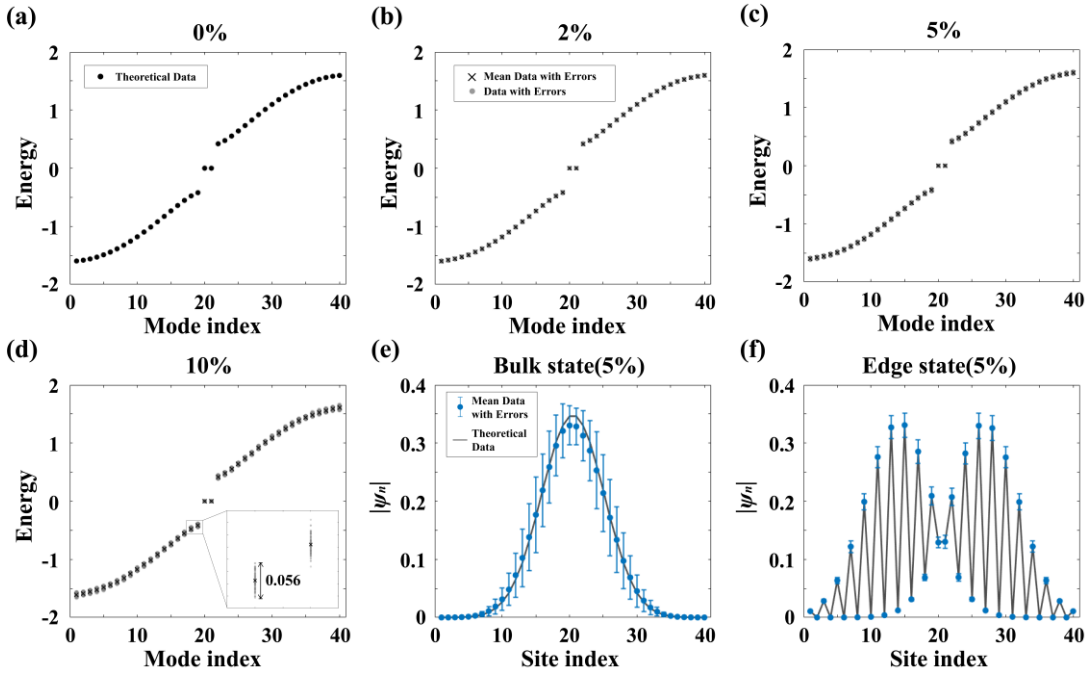

Figure S3. Robustness of the Topological SSH model against Random Errors under NHRE: **(a–d)** Incoherent mode distribution function for SSH models with hopping tolerances of 0%, 2%, 5%, and 10%, respectively. Gray points denote 100 independent disorder realizations, while black cross markers indicate the ensemble average; **(e, f)** Representative spatial profiles of **(e)** a bulk

state and **(f)** an edge state for the 5% tolerance level. The profiles are taken from individual disorder realizations and demonstrate that the in-gap edge-state energy and its spatial localization persist across all disorder strengths.

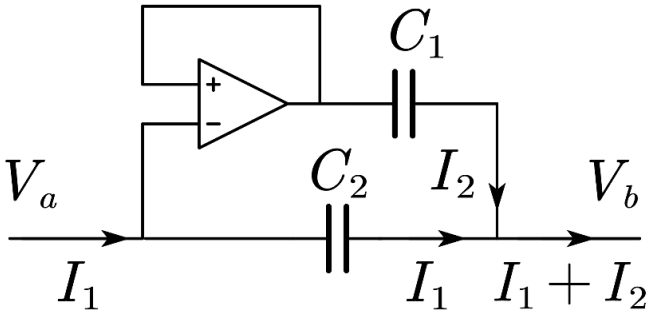

Figure S4. Generation of nonreciprocity in circuit system.

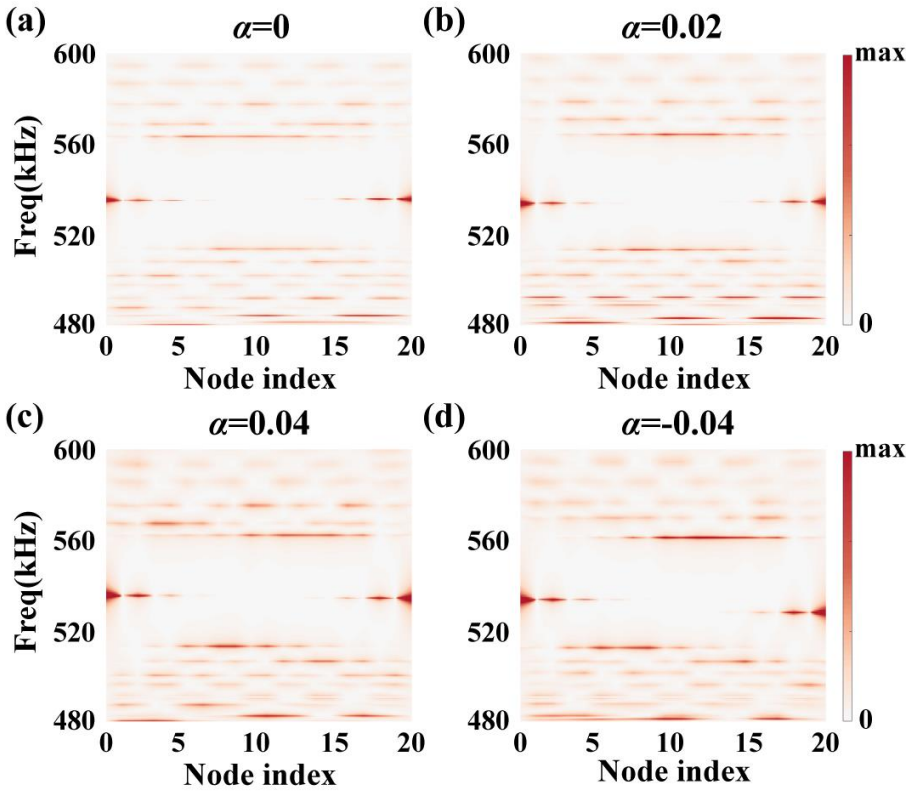

Figure S5. Measured Z_{aa} of the topological circuit at **(a)** $= 0$, **(b)** $\alpha = 0.02$, **(c)** $\alpha = 0.04$ and **(d)** $\alpha = -0.04$. The eigenstates remain delocalized in the non-Hermitian case, just as in the Hermitian scenario.

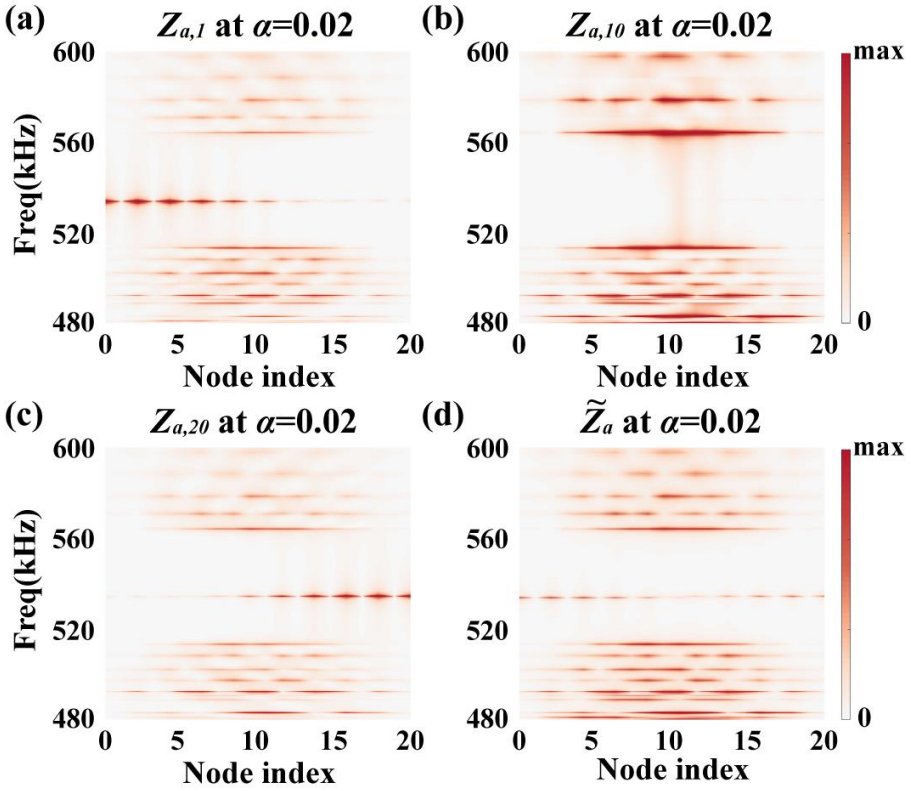

Figure S6. Measured mutual impedance spectra of the non-Hermitian topological circuit at $\alpha = 0.02$ for different excitation sites b: **(a)** $b = 1$, **(b)** $b = 10$, **(c)** $b = 20$, **(d)** summed over all b.

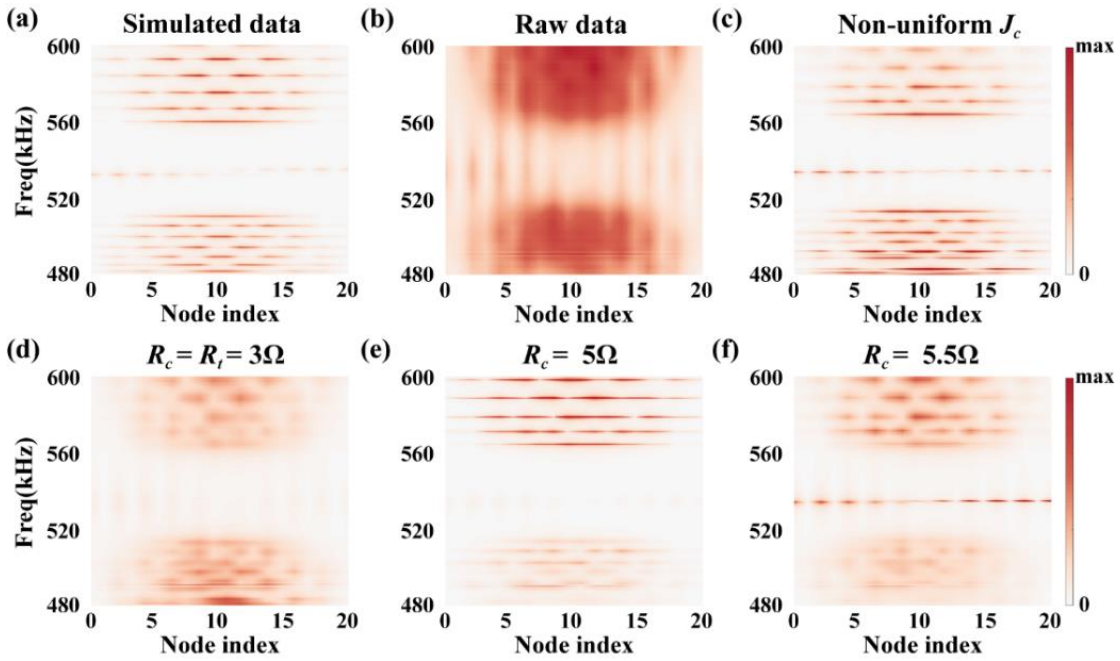

Figure S7. Comparison of two compensation methods for the $\tilde{Z}_a$ spectra in the non-Hermitian topological circuit: **(a)** Simulated data; **(b)** Raw experimental data; **(c)** Experimental data compensated via non-uniform $J_c(n, \omega)$, determined from the real part of J_{nn}; **(d–f)** Experimental data compensated via uniform J_c to account for the parasitic inductor resistance, with trial values: **(d)** $R_c = 3\ \Omega$, **(e)** $R_c = 5\ \Omega$, and **(f)** $R_c = 5.5\ \Omega$. The measured inductor resistance for a single loop is approximately $R_t \approx 3\ \Omega$.

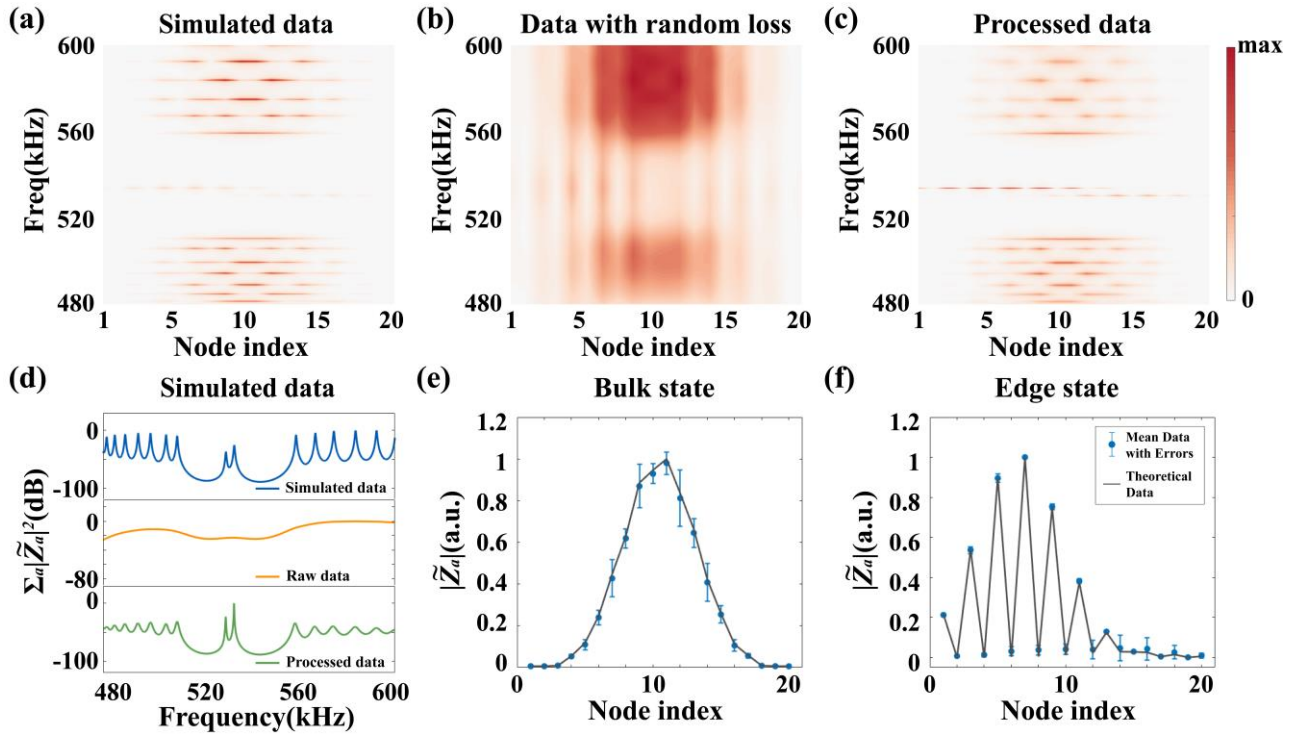

Figure S8. Numerical verification of the deterministic compensation method: **(a)** Numerically simulated spectrum of the summed mutual impedance $\tilde{Z}_a$ for the ideal lossless circuit; **(b)** Simulated $\tilde{Z}_a$ spectrum incorporating practical imperfections, including randomly distributed inductor parasitic resistance ($\sim$10% variation), randomly distributed capacitor parasitic resistance ($\sim$10% variation), capacitor tolerances ($\sim$1%), and measurement errors ($\sim$1%), exhibiting loss-induced broadening and significant mode overlap; **(c)** Processed $\tilde{Z}_a$ spectrum after applying the compensation procedure to the imperfect data in **(b)**, demonstrating clear resolution of individual eigenmodes; **(d)** Incoherent mode distribution function versus frequency, with peaks corresponding to resonant frequencies satisfying $E_n = \lambda(\omega_n)$; **(e, f)** Spatial profiles of representative **(e)** bulk and **(f)** edge states, showing theoretical predictions (dotted curves) alongside statistical results from multiple random realizations (ensemble averages and standard deviations). The consistency across different disorder realizations demonstrates the robustness and determinism of the compensation scheme.

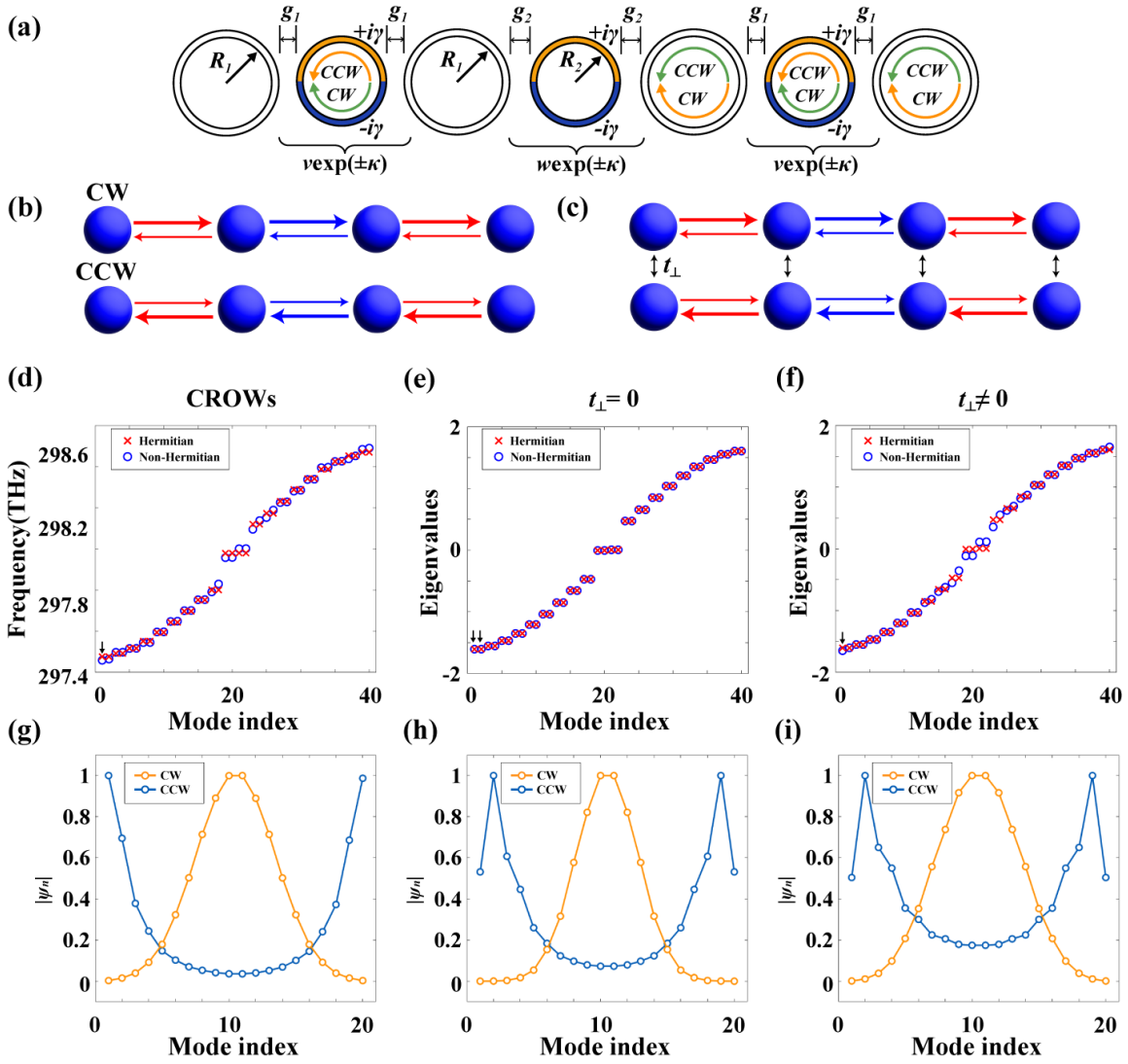

Figure S9. Verification of NHRE in CROWs: **(a)** Schematic of the CROW system; **(b)** Uncoupled and **(c)** coupled TBM SSH chains; **(d–f)** Eigenfrequencies of the CROWs and the two TBMs, comparing the Hermitian model (red cross) and the non-Hermitian model (blue circles); **(g–i)** Projected eigenstates of the non-Hermitian model corresponding to the CW and CCW modes for the eigenstate with the smallest real part of the eigenvalue.